

Multi-GNSS real-time tropospheric delay retrieval based on SSR products from different analysis centers

Wanqiang Yao¹, Haoran Huang¹, Xiongwei Ma¹, Qi Zhang², Yibin Yao², Xiaohu Lin¹, Qingzhi Zhao¹ and Yunzheng Huang¹

¹College of Geomatics, Xi'an University of Science and Technology, Xi'an 710054, China

²School of Geodesy and Geomatics, Wuhan University. Wuhan 430000, China

Correspondence: Qi Zhang (qizhangsgg@whu.edu.cn)

Abstract: The troposphere plays an important role in a range of weather and various climate changes. With the development of the Global Navigation Satellite System (GNSS), the zenith tropospheric delay (ZTD) inversion based on GNSS has become one of the common methods. Research on real-time precise point positioning (RT-PPP)-derived ZTD accuracies of SSR corrections from different analysis centers is important for earth observation correction, meteorological disaster forecasting, and warning with the increasing abundance of state-space representation (SSR) products obtained by the International GNSS Service analysis center. Therefore, accuracies and availability of real-time orbits and clock errors obtained by the Chinese Academy of Sciences (CAS), GMV Aerospace and Defense (GMV), Centre National d'Etudes Spatiales (CNE) and Wuhan University (WHU) are evaluated, and the RT positioning performance and ZTD accuracies are analyzed for GPS, Galileo, BDS3. The results indicate that CAS has the higher satellite availability, providing SSR corrections for 82 GPS, Galileo, BDS3 satellites. The accuracies of GPS/Galileo/BDS3 orbits are best at WHU, CAS, WHU with values of 5.57/5.91/11.77 cm, respectively; the standard deviations (STDs) of clock error are all better than 0.22/0.19/0.55 ns, and the root mean square errors (RMSEs) are better than 0.54/0.32/1.46 ns. CAS has the best Signal-In-Space Ranging Errors, followed by WHU, while CNE and GMV are worse. In the RT-PPP test, convergence times for CAS and WHU are 14.9 minutes and 14.4 minutes, respectively, with 3D positioning accuracy both around 3.3 cm, which is better than CNE and GMV. Among them, WHU-SSR has the higher accuracy of RT-PPP-derived ZTD with an RMSE of 6.06 mm and desirable availability with a completeness rate of 89%.

Keywords: GNSS, State space representation, Zenith tropospheric delay, Real-time PPP

1 INTRODUCTION

ZTD can be used for earth observation error correction(Kinoshita, 2022; Xiong et al., 2019; Zhu et al., 2022), including GNSS, very long baseline interferometry, interferometric synthetic aperture radar, and warning and forecasting of extreme natural disasters (Li et al., 2022; Li et al., 2021; Li et al., 2023; Yao et al., 2018). Besides, satellite signals are affected by refraction during pass through the troposphere, causing delay errors (Gao et al., 2021). The tropospheric delay can also be converted to obtain atmospheric precipitation water vapor, facilitating the research on scientific issues such as global atmospheric radiation,

36 energy balance, and water cycle (Edokossi et al., 2020; Lin et al., 2018; Ma et al., 2021; Pipatsitee et al.,
37 2023). Therefore, RT and high-precision ZTD can be used to provide rapid and accurate tropospheric
38 correction services in space geodesy while benefiting weather forecasting and climate change research
39 (Crocetti et al., 2024; He et al., 2024).

40 GNSS is an important means of water vapor detection and is increasingly important in short-term and near-
41 space forecasting (Eugenia Bianchi et al., 2016; Li et al., 2023; Li et al., 2015; Sha et al., 2024). GNSS-ZTD
42 retrieval has an excellent prospect for development due to the advantages of all-weather, RT, and high
43 accuracy (Hadas et al., 2020; Li et al., 2023; Lu et al., 2016; Pan et al., 2024). The double-difference algorithm
44 through GNSS networking and PPP is commonly used for ZTD retrieval (Stępniaak et al., 2022). PPP has a
45 broader range of applications, including timing, atmospheric modeling, and deformation monitoring, due to
46 the lower cost and one GNSS receiver (Ge et al., 2021; Liu et al., 2018; Wang et al., 2023). However, the
47 PPP technology relies on high-precision GNSS orbit and clock error products, typically released as final
48 precise post-processing products to the public (Li et al., 2022). A working group was established by the
49 International GNSS Service Analysis Center (IGS) to study GNSS RT data and launched an RT data service
50 in 2013 for high-precision RT-PPP applications (Gu et al., 2022). GNSS RT orbits and clock corrections are
51 made available to users based on the Internet through the Networked Transport of RTCM via Internet
52 Protocol (NTRIP) (Shu et al., 2024; Wang et al., 2018; Wang et al., 2018). The orbit accuracy of IGS real-
53 time products is better than 5 centimeters, with a satellite clock error RMSE of approximately 0.15
54 nanoseconds, which is about 10 times better than the predicted portion of ultra-rapid clock deviations. (Di et
55 al., 2020). SSR products have led to a remarkable 50% improvement in RT-PPP positioning accuracy
56 compared to IGS ultra-fast products (Elsobeiey et al., 2016). SSR products are becoming increasingly
57 abundant with the rapid development of computer arithmetic and the increasing demand for real-time high-
58 precision GNSS applications. Li and Wang (Li et al., 2022) conducted a comprehensive evaluation of SSR
59 products from 10 analysis centers multi-GNSS and performed RT dynamic PPP, which showed the most
60 complete and highest quality products obtained by CNES and WHU. Furthermore, it has also been applied
61 to RT deformation monitoring, RT atmospheric detection, and other fields (Li et al., 2023). Capilla et al.
62 (2016) applied RT-PPP to deformation monitoring and demonstrated that the technique has a monitoring
63 accuracy of 2 cm and proved that RT-PPP was full of potential for deformation monitoring applications. Li
64 et al. (2015) investigated the ZTD solution and Integrated Water Vapor retrieval of multi-GNSS RT-PPP.
65 They compared RT-PPP-derived ZTD with data from concurrent radiosonde stations and very long baseline
66 interferometry, which demonstrated that the performance of the multi-GNSS RT-PPP-derived ZTD can reach
67 the millimeter level and has potential in the application of meteorology.

68 Researchers have assessed the accuracy of single-system RT-PPP-derived ZTD and multi-GNSS RT-PPP-
69 derived ZTD. Lu et al. (2015) found that the retrieval accuracy of atmospheric water vapor can be improved
70 by several millimeters when a combined GPS and BDS solution is used. Li et al. (2015) obtained RT-PPP-
71 derived ZTD using GPS, BDS2, Galileo, and GLONASS PPP, demonstrating higher accuracy and greater
72 ZTD availability than a single-system PPP. Jiao et al. (2019) analyzed the results of PPP and multi-GNSS

73 PPP, noting that the positioning accuracy and convergence were significantly improved with the inclusion of
74 the BDS3 satellite system. The accuracy of BDS3-derived ZTD is improved by 20.5% versus that of BDS2.
75 Alcay et al. (2021) compared the GPS-, GPS/GLONASS- and GPS/GLONASS/Galileo/BDS-PPP solutions
76 and found that the ZTD difference between the three schemes was less than 20 mm. Lu et al. (2017) compared
77 the accuracy of the RT-PPP-derived ZTD using the different SSR products, and the multi-GNSS RT-PPP-
78 derived ZTD based on GFZC2 SSR products showed the highest accuracy.

79 The ongoing discussion primarily centers on the influence of single- and multi-GNSS RT-PPP on the
80 accuracy of RT ZTD. Yet, there is a limited discourse on the influence of the different analysis centers-based
81 SSR corrections on the accuracy of RT ZTD. The quality of GNSS SSR products has improved with the
82 increasing abundance of SSR products provided by IGS. Most studies have focused on BDS2 (Lu et al., 2015;
83 Pan et al., 2018), while BDS3 needs to be sufficiently studied. Moreover, evaluating the influence of different
84 GNSS SSR products for the accuracy of RT-PPP-derived ZTD is an important reference value for achieving
85 high-precision and high-availability in RT-PPP-derived ZTD with the growth of SSR products. In this study,
86 positioning performance and ZTD accuracy are estimated using the RT-PPP based on multi-GNSS from 8
87 IGMAS stations from 355 in 2023 to 14 in 2024. Our primary objective is to compare the RT-PPP positioning
88 performance, RT-PPP-derived ZTD accuracy and availability based on SSR products from different analysis
89 centers. The findings serve as a valuable reference for selecting SSR products in RT-PPP-derived ZTD and
90 hold significant importance for applications such as earth observation correction, meteorological disaster
91 prediction, etc.

92 **2 THE METHOD OF RT-PPP-DERIVED ZTD**

93 **2.1 Data collection**

94 IGS was established to bolster geodetic and geodynamic research, officially launching its operations on
95 January 1, 1994. IGS offers worldwide access to GNSS satellite observations from various tracking stations
96 and products, including satellite ephemerides, clock errors, earth orientation parameters, atmospheres, etc.
97 (Geng et al., 2021; Griffiths, 2019). IGMAS was established under the leadership of China in 2012. Its
98 primary purpose is establishing an information platform equipped with data acquisition, storage, analysis,
99 management, and release functions for the global RT tracking network of the four major satellite navigation
100 systems with full arcs and multiple coverage observations. The leading indicators and operational status of
101 GNSS are tested and assessed to generate products such as high-precision precision ephemerides, satellite
102 clock errors, geotropic parameters, tracking station coordinates and rates, and global ionospheric delays(Li
103 et al., 2022; Zhang et al., 2023).

104 The workflow of this study is shown in Figure 1 and includes three parts: verifying the performance of
105 PPP, assessing different SSR products, and verifying the performance of RT-PPP using the results obtained
106 by post-processing PPP and PRIDE PPPAR. PRIDE PPPAR is a multi-GNSS real-time PPP open-source
107 software developed by the Pride Laboratory at Wuhan University. The software supports the post-processing
108 of multi-system GNSS data and can be applied to various fields, including geodesy, seismic analysis,

109 photogrammetry, gravity measurement, and other research areas. In the first part, the position and ZTD are
 110 estimated using the multi-GNSS post-processing PPP technique from IGS stations in Asia-Pacific to verify
 111 the performance of multi-GNSS post-processing PPP. A total of 20 stations are selected in countries such as
 112 Mongolia, Russia, Japan, India, Thailand, and others. The 14 IGS sites with the highest availability are
 113 selected from the IGS sites for experimental analysis according to the number of observation documents. In
 114 the second part, the accuracies of SSR products from four analysis centers are evaluated. In the third part, the
 115 position and ZTD are estimated using a multi-GNSS RT-PPP technique from 8 IGMAS stations in China.
 116 Data from DOY 355 in 2023 to DOY 14 in 2024 are utilized. GPS, Galileo, and BDS3 can be received at
 117 these stations simultaneously. The solutions obtained by PRIDE PPPAR and post-processing PPP are
 118 considered the reliable position and ZTD to verify the performance of RT-PPP. Figure 2 displays the
 119 distribution information of the selected IGS and IGMAS sites in this study and the information of IGMAS
 120 stations is shown in Table 1. It should be noted that "IGS" refers to all IGS stations in China and the
 121 surrounding areas, while "IGS Stations for PPP validation" refers to the specific IGS stations selected for
 122 study.

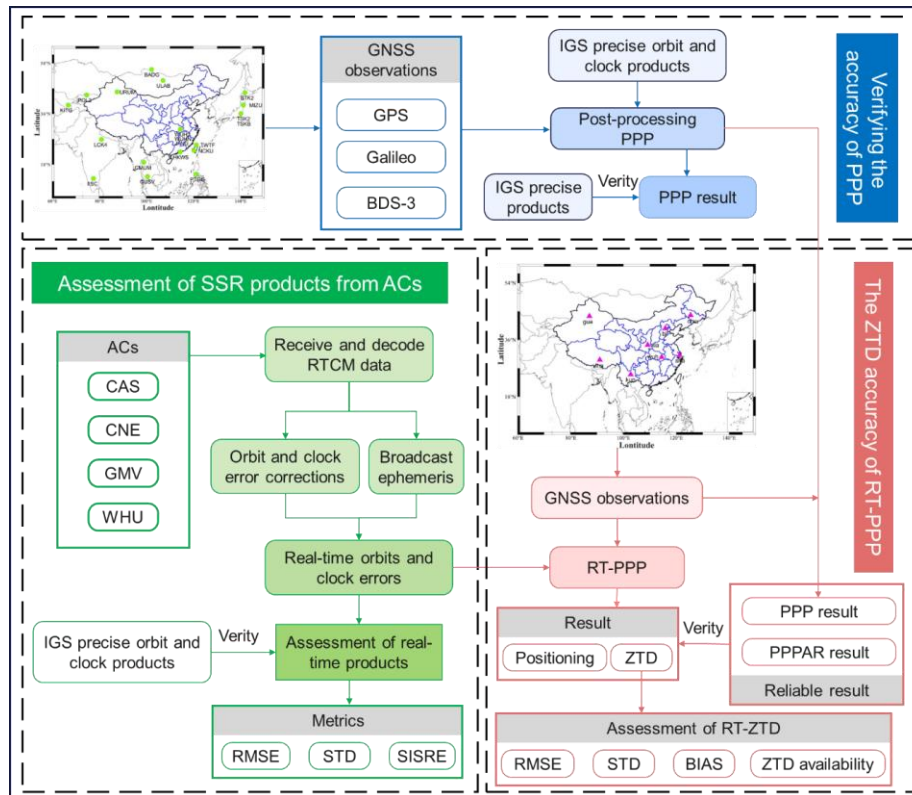


Figure 1. The workflow of this study.

Table 1. Location information of IGMAS stations.

Stations	Longitude/°	Latitude/°	Height/m	Geographical area
BJF	115.89	39.61	75.4	North China
CHU	125.44	43.79	273.9	Northeast Region

GUA	87.18	43.47	2029.3	Northwest China
KUN	102.80	25.03	1988.4	Southwest China
LHA	91.10	29.66	3630.2	Southwest China
SHA	121.20	31.10	20.9	East China
WUH	114.49	30.52	71.1	Central China
XIA	109.22	34.37	449.4	Northwest China

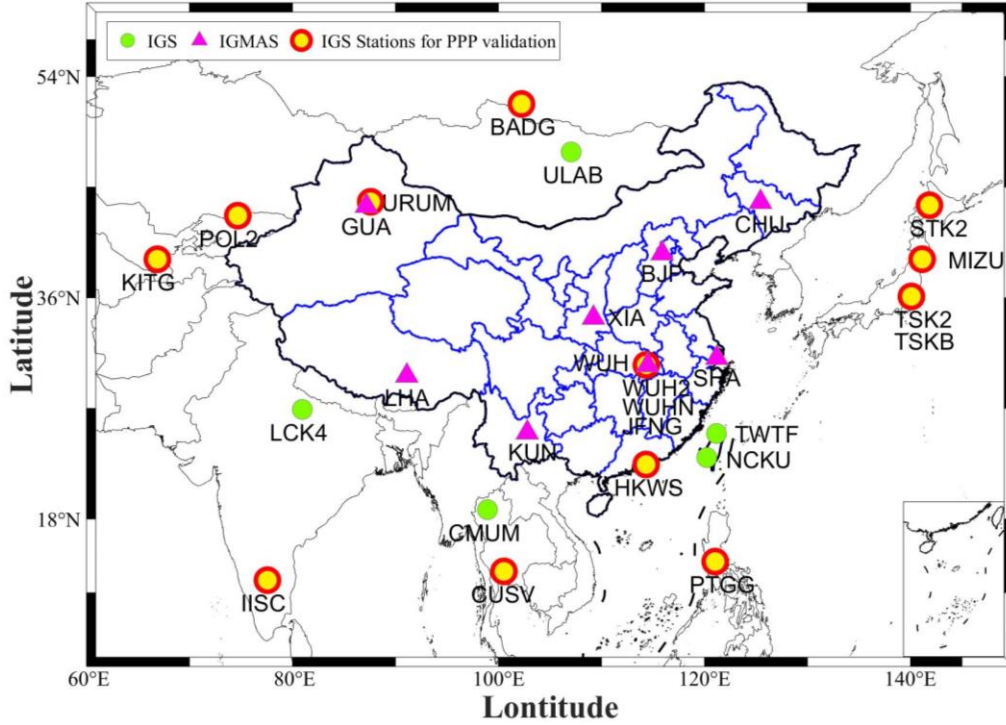


Figure 2. The distribution of IGMAS stations and IGS stations.

2.2 Recovering real-time products

IGS RT satellite orbit correction includes the position correction $dO = [\delta O_r, \delta O_a, \delta O_c]^T$ and velocity correction $d\bar{O} = [\delta \bar{O}_r, \delta \bar{O}_a, \delta \bar{O}_c]^T$ at the reference moment t_0 ; then the orbital correction at the moment t is:

$$\delta O = O + d\bar{O}(t - t_0) \quad (1)$$

The orbital corrections from the spacecraft body-fixed system should be transformed to the Earth-Centered Earth-Fixed system by means of a coordinate transformation. Since the positioning is usually done in the Earth-Centered Earth-Fixed:

$$X = \begin{bmatrix} \frac{\bar{r}}{|\bar{r}|} \times \frac{r \times \bar{r}}{|r \times \bar{r}|} & \frac{\bar{r}}{|\bar{r}|} & \frac{r \times \bar{r}}{|r \times \bar{r}|} \end{bmatrix} \delta O \quad (2)$$

137 where $r = X_{brdc}$ refers to satellite positions from broadcast ephemeris. $\bar{r} = \bar{X}_{brdc}$ refers to velocity from
 138 broadcast ephemeris. The X_{pre} refers to precise satellite position, which can be calculated by:

$$139 \quad X_{pre} = X_{brdc} - \delta X \quad (3)$$

140 The RT correction of the clock error refers to the difference of precision clock error δt_{pre} versus broadcast
 141 clock error δt_{brdc} , which is similar to RT orbital correction. However, the SSR clock error correction is
 142 represented by c_0 , c_1 , and c_2 of the reference time t_0 unlike orbital corrections and the RT correction δc
 143 is obtained by fitting c_0 , c_1 , and c_2 . The RT correction δc of the clock error at the moment t is:

$$144 \quad \delta c = c_0 + c_1(t - t_0) + c_2(t - t_0)^2 \quad (4)$$

145 Eventually, precision clock errors δt_{pre} are obtained by:

$$146 \quad \delta t_{pre} = \delta t_{brdc} - \delta c / C_{light} \quad (5)$$

147 where δt_{brdc} and C_{light} refers to clock error from broadcast ephemeris and speed of light.

148 2.3 PPP functional model

149 The impacts of satellite orbits and clock errors are mitigated by employing RT satellite orbits and clock
 150 errors recovered by SSR in the PPP technique. ZTD is solved as an unknown parameter of the equation. The
 151 principle is to construct two observation equations based on the ionosphere-free (IF) combinations of pseudo-
 152 range and carrier phase observation (Ju et al., 2022; Ke et al., 2020). The basic observation equations can be
 153 expressed as follows:

$$154 \quad \begin{cases} P_{r,i}^s = \rho_{r,i}^s + C_{light}(dt_r - dt^s) + I_{r,i}^s + T_r^s + b_{r,i}^s + b_{r,i}^s + \varepsilon_{r,p}^s \\ L_{r,i}^s = \rho_r^s + C_{light}(dt_r - dt^s) - I_{r,i}^s + T_r^s + \lambda_i N_{r,i}^s + \delta_{r,i} - \delta_{r,i}^s + \varepsilon_{r,\phi}^s \end{cases} \quad (6)$$

155 where s refer to the satellites. r refer to the receiver. and i refer to the frequency. $L_{r,j}^s$ and $P_{r,j}^s$ are the
 156 carrier phase and pseudo-range observation from receiver r to satellite S , respectively. ρ refers to the
 157 satellite-receiver geometric distance. dt_r is the receiver clock error and dt^s is the satellite clock error. I is
 158 the Ionospheric delay. T_r^s refers to the tropospheric delay. λ is the wavelength. δ and b denote the phase
 159 delays and the code biases, respectively. N is the integer ambiguity. $\varepsilon_{r,p}^s$ is the pseudo-range observation
 160 noise. $\varepsilon_{r,L}^s$ is carrier phase observation noise.

161 The dual-frequency IF combination model is constructed and simplified from the equation(6):

$$162 \quad \begin{cases} P_{IF} = \rho - cdt + T_r^s + \varepsilon_{r,s}^s \\ L_{IF} = \rho - cdt + T_r^s + \lambda_1 N_{IF} + \varepsilon_{r,\phi}^s \end{cases} \quad (7)$$

163 where L_{IF} is the carrier phase observation. P_{IF} is the pseudo-range observation. The unknown parameters
 164 can be estimated in IF-PPP are as follows:

$$X = \begin{bmatrix} x & cd\bar{t}_r & Z & \bar{N}_{IF}^s \end{bmatrix} \quad (8)$$

165

166 where x is the position of the receiver. $cd\bar{t}_r$ refers to receiver clock error. Z refers to the Tropospheric167 delay. \bar{N}_{IF}^s refers to the integer phase ambiguity.168 **2.4 Accuracy evaluation**

169 Two methods are used to evaluate the accuracy of RT-PPP-derived ZTD at IGMAS stations. The first is
 170 our post-processing PPP based on RTKLIP for secondary development, and the other one is PRIDE PPPAR
 171 from Geng et al. of Wuhan University. The consistency between the solution data and the IGS precision
 172 products is used to evaluate the positioning and ZTD accuracy of post-processing PPP for IGS stations. Gross
 173 errors and outages in the RT clock error products will lead to an unreliable accuracy assessment of the RT
 174 clock error products. The accuracy statistics of clock error may be affected if a single satellite's clock error
 175 is used as the reference. Therefore, the average satellite clock error at the current epoch is used as a reference
 176 to eliminate system errors in this study(Yao et al., 2017). The root mean square error (RMSE), STD, and bias
 177 of the differences are used to evaluate SSR products and positioning and ZTD of RT-PPP. The three metrics
 178 are calculated as follows(Su et al., 2023):

$$\begin{cases} RMSE = \sqrt{\frac{1}{N} \sum_{i=1}^N \Delta^2} \\ STD = \sqrt{\frac{1}{N} \sum_{i=1}^N (\Delta - \Delta_{ave})^2} \\ BIAS = \frac{1}{N} \sum_{i=1}^N \Delta \end{cases} \quad (9)$$

179

180 where N is the sample number. Δ is the difference of the SSR products versus the IGS precision products.181 Δ_{ave} is the average Δ .

182 The Pearson correlation coefficient (R) is also used to evaluate the consistency of reliable ZTD and RT-
 183 PPP-derived ZTD. R is calculated as follows:

$$R = \frac{\sum_{i=1}^N \left(ZTD_i^{der} - \overline{ZTD_i^{der}} \right) \left(ZTD_i^{ref} - \overline{ZTD_i^{ref}} \right)}{\sqrt{\sum_{i=1}^N \left(ZTD_i^{der} - \overline{ZTD_i^{der}} \right)^2 \sum_{i=1}^N \left(ZTD_i^{ref} - \overline{ZTD_i^{ref}} \right)^2}} \quad (10)$$

184

185 where ZTD_i^{der} is the PPP solution results; ZTD_i^{ref} refers to the tropospheric delay used as a reference.186 $\overline{ZTD_i^{der}}$ and $\overline{ZTD_i^{ref}}$ denote the mean of ZTD_i^{der} and ZTD_i^{ref} respectively.

$$E_{SISRE} = \sqrt{\left[RMSE(\omega_R \Delta r_R - C_{light} \Delta C) \right]^2 + \omega_{A,C}^2 \left\{ \left[RMSE(\Delta r_A) \right]^2 + \left[RMSE(\Delta r_C) \right]^2 \right\}} \quad (11)$$

187

188 where E_{SISRE} refers to the Signal-In-Space Ranging Errors (SISRE); ΔC is the difference of the RT clock
 189 error versus the IGS precision products in each epoch; Δ_{r_R} , Δ_{r_A} , and Δ_{r_C} are orbital errors in the radial, along-

190 track, and cross-track (R/A/C) direction in each epoch, respectively. ω_R and $\omega_{A,C}^2$ are weighting factors that

191 convert the orbital errors in the R/A/C direction to the orbital errors in the line-of-sight direction(Kazmierski
192 et al., 2020). Different Satellite systems have different SISRE weighting factors, as shown in Table 2.

193

Table 2 Weight factors of SISRE

Satellite system	ω_R	$\omega_{A,C}^2$
GPS	0.98	1/49
Galileo	0.98	1/61
BDS (MEO)	0.98	1/54
BDS (IGSO, GEO)	0.99	1/126

194 3 ACCURACY EVALUATION OF SSR PRODUCTS

195 The stability of SSR streams can be influenced by various factors, including the receiving software,
196 network stability, and the broadcasting organization. In this study, RTKNAVI software is used to receive the
197 SSR products in the same network environment from the mount-points of SSRC00CAS0, SSRC00CNE0,
198 SSRC00GMV0, and SSRC00WHU0. Since the real-time data from other analysis centers are incomplete
199 during the DOY 355 in 2023 to DOY 14 in 2024, the SSR data from 4 analysis centers are used in this study.
200 The SSR product information for each subsystem center is shown in Table 3.

201

Table 3. RTCM-SSR mount points Description.

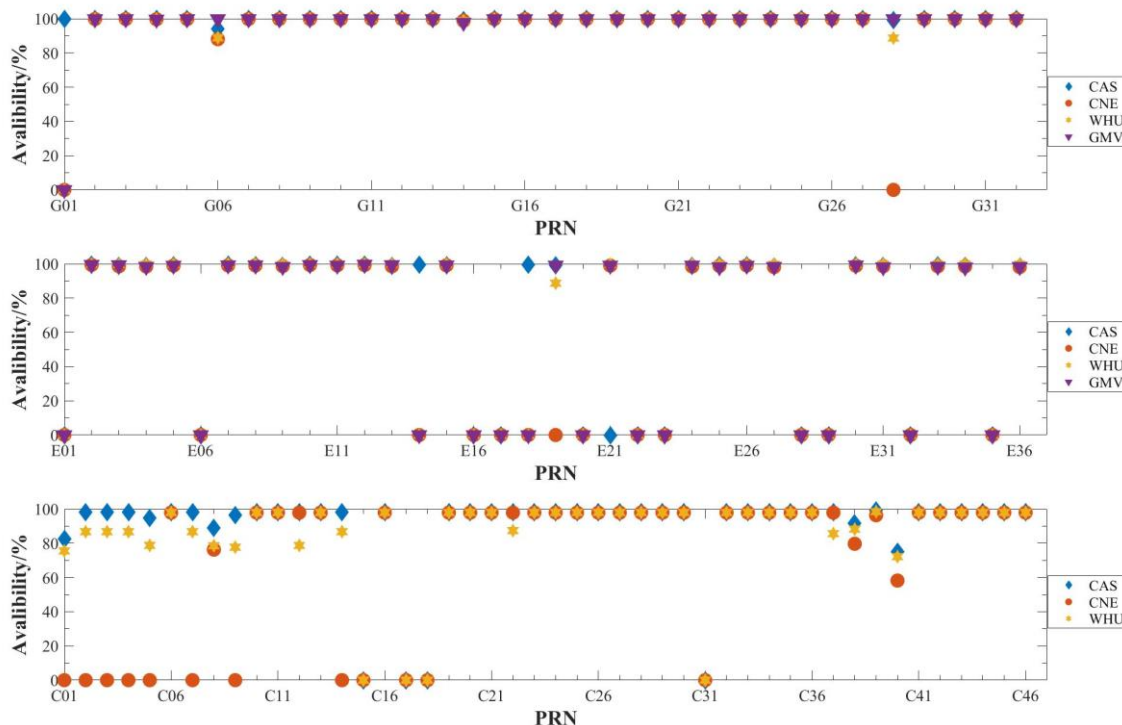
analysis center	Name of Institutions	Mount-points	Supported systems	Update Interval of Orbit/s	Update Interval of Clock/s	Reference Point
CAS	Chinese Academy of Sciences Centre	SSRC00CAS0	GPS+GLO+GAL+BDS	5	5	CoM
CNE	National d'Etudes Spatiales GMV	SSRC00CNE0	GPS+GLO+GAL+BDS	5	5	CoM
GMV	Aerospace and Defense	SSRC00GMV0	GPS+GLO+GAL+BDS	5	5	CoM
WHU	Wuhan University	SSRC00WHU0	GPS+GLO+GAL+BDS	5	5	CoM

202 3.1 SSR Products availability

203 The SSR product completeness rates for the four analysis centers are assessed for 26 days, from DOY 355
204 in 2023 to 14 in 2024, as illustrated in Figure 3. Notably, this study excludes the unhealthy satellite G01 from
205 consideration. Since SSR corrections for 31 GPS satellites, 24 Galileo satellites, and 27 BDS3 satellites can
206 be obtained, CAS has the higher satellite availability. WHU offers SSR corrections for 31 GPS satellites, 23
207 Galileo satellites, and 27 BDS3 satellites. CNE demonstrates lower availability, providing 30 GPS satellites,
208 22 Galileo satellites, and 27 BDS3 satellites. GMV provides SSR corrections for 31 GPS satellites and 23
209 Galileo satellites. BDS-SSR products obtained by GMV are unavailable due to software decoding issues with
210 GMV-SSR products during the experimental data period of this study, which resulted in pseudo-random

211 noise and issue of data ephemeris errors for its BDS satellites. Although the variation of epoch availability
 212 for GPS, Galileo, and BDS3 SSR corrections from different analysis centers is different, the average epoch
 213 availability of the SSR products provided by the four analysis centers is above 97.5%.

214



215

216

Figure 3. Epoch availability of SSR corrections during the experiment.

217

3.2 Accuracy of SSR products

218

219

220

221

222

223

224

225

226

227

228

229

230

231

IGS precision products are chosen as references to evaluate different SSR products. The RMSEs of GPS RT orbits in the R/A/C directions for the four analysis centers are shown in Figure 4. The average RMSEs of GPS, Galileo, and BDS3 RT orbits in the R/A/C directions are shown in Table 4. Figure 4 and Table 4 show that the RMSEs of orbit products in the R-direction are mostly smaller than in the C-direction, with the RMSEs of orbit products in the R-direction being the largest due to the observation being mainly centered around the R-direction. The accuracies of GPS, Galileo, and BDS3 RT orbits from different analysis centers are individually evaluated. The accuracies of GPS RT orbits from four analysis centers reach the centimeter level and WHU has the best accuracy, followed by CAS and GMV. GPS RT orbits from CNE are relatively worse, with 8.09 cm. Galileo RT orbits from CAS exhibit the lowest error, followed by WHU and GMV, with CNE showing relatively worse accuracy with 10.28 cm. The accuracies of BDS3 RT orbits from four analysis centers are better than 17 cm. The accuracy of BDS3 RT orbits from WHU is the best, CAS is the second with 14.18 cm, and the products from CNE are worse, with 16.42 cm. Overall, Galileo RT orbits from CAS display the best accuracy, with 5.91 cm, while WHU has the best accuracies of GPS and BDS3 RT orbits, with 5.57 cm and 11.77 cm, respectively.

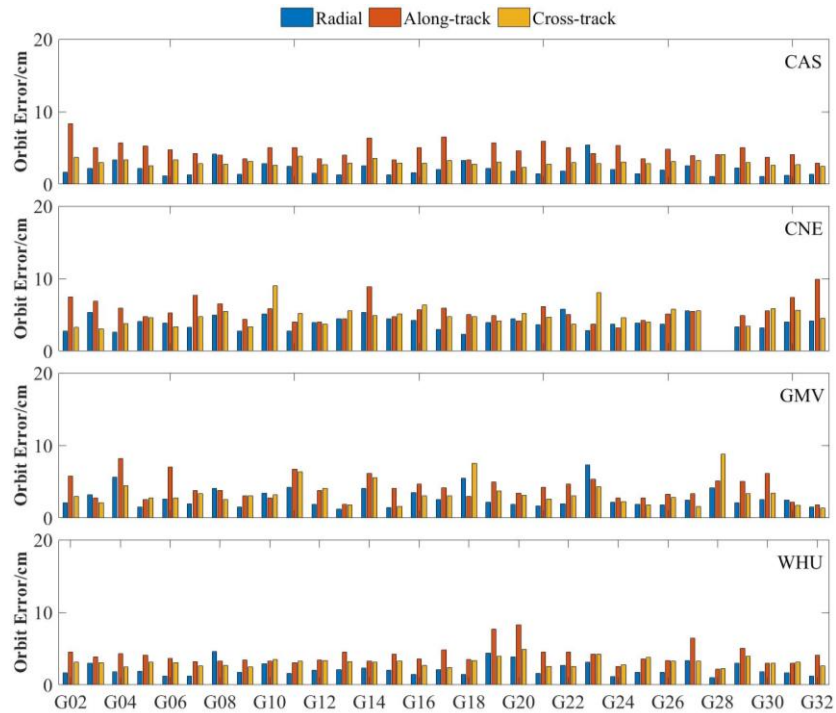


Figure 4. The RMSE values in R/A/C directions of GPS RT orbit from different analysis centers.

Table 4. The mean accuracies of GPS, Galileo, and BDS3 RT precise products from different analysis centers /cm.

		R	A	C	3D			R	A	C	3D
CAS	GPS	2.07	4.68	3.08	5.97	CNE	GPS	3.82	5.28	4.80	8.09
	GAL	1.91	4.67	3.09	5.91		GAL	6.92	5.70	5.02	10.28
	BDS3	6.67	10.32	7.08	14.18		BDS3	5.50	12.57	9.02	16.42
GMV	GPS	2.82	4.40	3.54	6.31	WHU	GPS	2.20	4.06	3.13	5.57
	GAL	2.18	6.59	3.61	7.82		GAL	2.73	5.31	4.20	7.30
	-	-	-	-	-		BDS3	5.30	8.41	6.31	11.77

Figure 5 displays the RMSEs and STDs of GPS RT clock errors from four analysis centers. Table 5 shows the RMSEs and STDs of GPS, Galileo, and BDS3 RT clock errors. The RT clock errors of G03 provided by CNE and WHU are excluded from this study due to their gross errors. The remaining GPS satellites are used commonly. The mean STDs of GPS RT clock errors from CAS, GMV, and CNE are 0.16, 0.19, and 0.14 ns, respectively, with the largest STD from WHU being 0.22 ns. For Galileo, CAS RT clock errors display the best accuracy, with a mean STD of 0.11 ns. For BDS3, WHU RT clock errors have the best accuracy with STD of 0.39 ns. Overall, the mean STDs of GPS, Galileo, and BDS3 from the three analysis centers are better than 0.22, 0.19, and 0.55 ns, respectively, and the mean RMSEs of GPS, Galileo, and BDS3 from these analysis centers are better than 0.54, 0.32, and 1.46 ns, respectively.

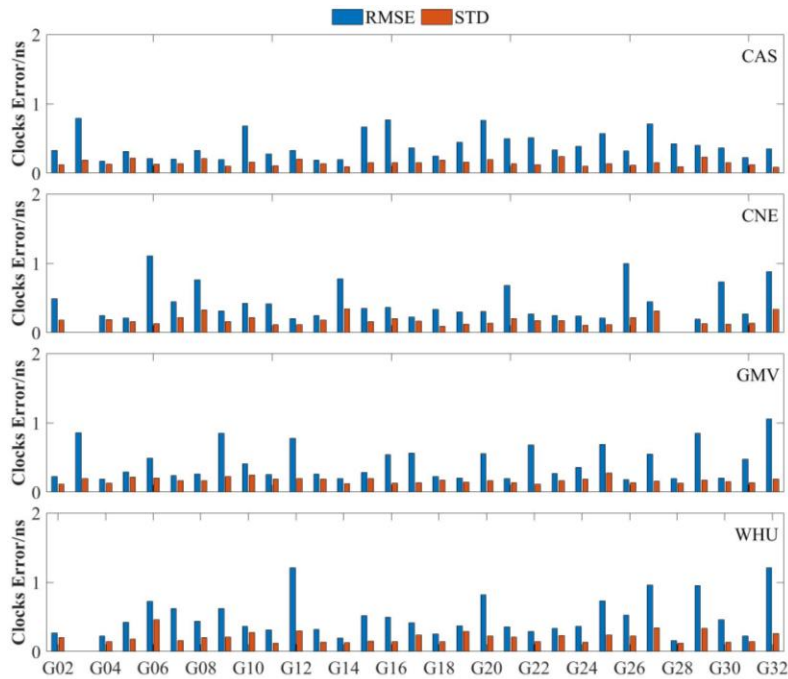


Figure 5. The RMSEs and STDs of GPS RT clock errors from different analysis centers.

Table 5. The mean accuracies of GPS, Galileo, and BDS3 RT precise products from different analysis centers /cm.

		RMSE	STD			RMSE	STD
CAS	GPS	0.38	0.16	CNE	GPS	0.41	0.19
	GAL	0.17	0.11		GAL	0.32	0.17
	BDS3	1.03	0.41		BDS3	1.76	0.84
GMV	GPS	0.38	0.14	WHU	GPS	0.54	0.22
	GAL	0.21	0.19		GAL	0.24	0.14
-	-	-	-		BDS3	1.02	0.39

3.3 Accuracy of SISRE

Table 6 shows the average SISREs of GPS, Galileo, and BDS3 from four analysis centers. For GPS, the order of magnitude of SISREs for different analysis centers is WHU>CNE>GMV>CAS. For Galileo, CAS and WHU have the better SISRE with around 5 cm and CNE has the worst SISRE with 9.80 cm. For BDS3, the SISREs of CAS and WHU are significantly better than the SISRE of CNE, which are 29.11, 29.98, and 57.48 cm, respectively. Overall, CAS has the best SISREs of GPS, Galileo, and BDS3, followed by WHU as the second, while CNE and GMV exhibit the worst accuracy.

Table 6. Mean SISRE of GPS, BDS, and BDS3 satellite of SSR products from different analysis centers /cm.

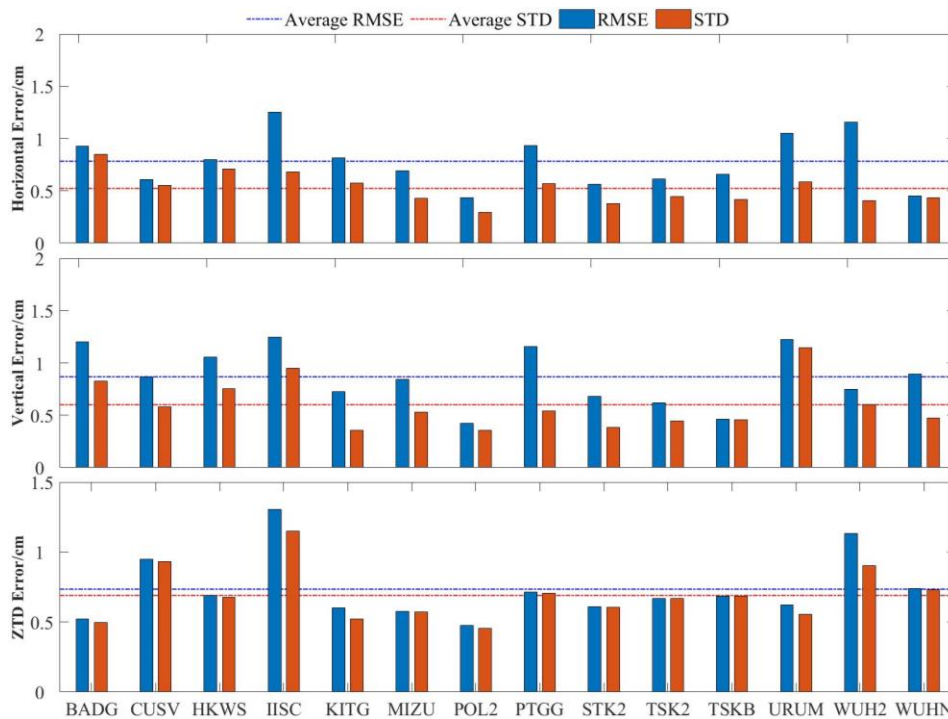
		SISRE			SISRE
CAS	GPS	9.50	CNE	GPS	11.06
	GAL	4.91		GAL	9.80
	BDS3	29.11		BDS3	57.48

GMV	GPS	10.44	WHU	GPS	12.55
	GAL	6.64		GAL	4.93
	-	-		BDS3	29.98

258 4 RESULT

259 4.1 Performances of multi-GNSS PPP at IGS stations

260 IGS post-processed precise position and ZTD products are used to evaluate the multi-GNSS post-
 261 processing PPP performance at 14 IGS sites in and around China. The average convergence time of all
 262 stations are less than 20 minutes. The station coordinates from the IGS SINEX files and the ZTD from the
 263 IGS ZPD files are used as references. Positioning performance and ZTD accuracy of post-processing PPP
 264 are shown in Figure 6. The RMSEs of horizontal and vertical errors are within 15 mm for all sites, respectively.
 265 The RMSEs of ZTD are within 10 mm for most sites, with an average RMSE of 7.4 mm. The abovementioned
 266 results suggest that post-processing PPP demonstrates good performance in both positioning and ZTD and
 267 can be used to verify the performance of RT-PPP.



268
 269 Figure 6. RMSEs and STDs of the positioning performance and ZTD accuracy of post-processing PPP,
 270 respectively.

271 4.2 RT-PPP with SSR products from different analysis centers in the IGMAS station

272 4.2.1 Convergence time of RT-PPP

273 To assess the accuracy of four SSR products, the eight IGMAS stations are selected for RT-PPP after
 274 verifying the performance of post-processing PPP. The testing period spans from DOY 355 in 2023 to DOY
 275 14 in 2024. The LHA is excluded due to a low number of observations among the eight IGMAS stations. The

276 IF model is used. A larger Cut-off elevation than the usual cut-off angle can be used when using multi-system
 277 PPP (Teunissen et al., 2014). Therefore, the 10° is selected as the Cut-off elevation in this study. The Kalman
 278 filter is used to estimate parameter, and additional positioning strategies are presented in Table 7.

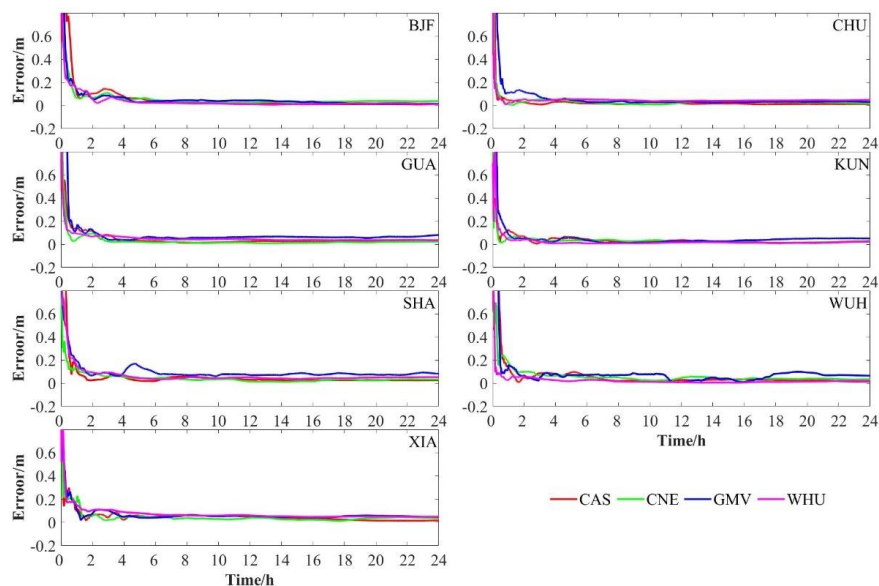
279

Table 7. Strategies for RT-PPP.

Items	Correction model or estimation strategy
Estimator	Kalman filter
Observations	IF code and phase combinations
Sampling rate	30 s
Cut-off elevation	10°
Phase-windup effect	Corrected
Tropospheric delay	Saastamoinen
Ionospheric delay	Estimated as a random-walk noise process
Relativistic effects	Eliminated by IF combination
antenna phase center	Corrected
Orbit and clock product	igs14.atx
Phase ambiguities	SSR corrections + broadcast ephemeris
	Float

280

281 The convergence time, positioning, and ZTD accuracies for multi-GNSS RT-PPP are assessed based on
 282 the different SSR products. The convergence time is the initial epoch where the error of horizontal and
 283 vertical direction are both less than 10 cm, holding for 20 epochs. Figure 7 shows multi-GNSS RT-PPP
 284 positioning errors in the 3D direction using the SSR products from the four analysis centers at seven stations
 285 on DOY 12, 2024. The results of RT-PPP from different analysis centers are represented by distinct colors,
 286 respectively, and the seven sub-figures represent the seven IGMAS sites, respectively. The sub-figures are
 287 set with the same range of vertical axes for comparison and the X direction is the hour since the start of the
 288 solution. The average convergence time of four analysis centers is less than 30 min, and the 3D positioning
 289 accuracies of four analysis centers are better than 10 cm after completing the convergence process.

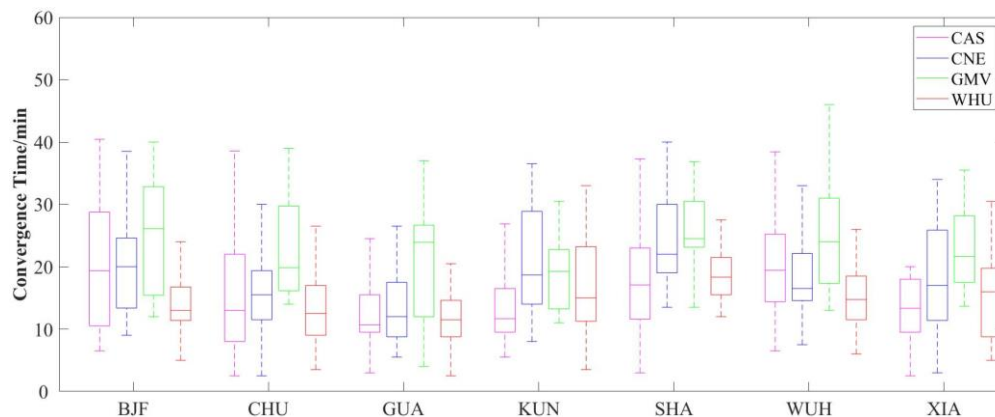


290

291

Figure 7. RT-PPP errors of different analysis centers at seven IGMAS stations.

292 The convergence time for seven stations over 26 days from four analysis centers is counted. Figure 8 shows
 293 box plots of the convergence time, including the median, 25% quantile, and 75% convergence time. Table 8
 294 provides a detailed breakdown of convergence time statistics for four analysis centers. The average
 295 convergence time at all sites based on CAS, WHU, and CNE is less than 20 min, while GMV is 22.8 min.
 296 The discrepancy in the convergence time from GMV and other analysis centers may be because that RT-PPP
 297 based on GMV-SSR products only uses GPS and Galileo, with fewer satellites than the other analysis centers.
 298 The average convergence time for CAS and WHU are similar with 14.9 min and 14.4 min, respectively, and
 299 for CNE is 17.4 min, which is slightly longer than CAS and WHU because CNE has fewer satellites available
 300 than CAS and WHU.



301

302

Figure 8. Boxplot of the convergence time of different analysis centers at IGMAS stations.

303

Table 8. The MAX, MIN, and MEAN of the convergence time derived from RT-PPP of different analysis centers /min.

304

analysis center	Stations	MAX	MIN	MEAN	Stations	MAX	MIN	MEAN
CAS	BJF	40.0	6.5	19.4	CHU	45.0	3.0	13.0
	GUA	31.0	3.0	10.7	KUN	45.0	5.5	11.7
	SHA	43.5	3.5	17.1	WUH	35.0	6.5	19.4
	XIA	40.5	5.0	13.3	Mean	40.0	4.7	14.9
	BJF	39.5	6.0	20.0	CHU	26.0	3.0	15.5
CNE	GUA	25.5	3.5	12.0	KUN	46.0	6.5	18.7
	SHA	38.0	15.5	22.0	WUH	39.5	6.0	16.5
	XIA	31.0	3.0	17.0	Mean	35.1	6.2	17.4
	BJF	40.0	12.0	26.1	CHU	39.0	14.0	19.8
GMV	GUA	37.0	5.0	23.9	KUN	30.5	11.0	19.3
	SHA	36.0	13.5	24.5	WUH	46.0	13.0	24.0
	XIA	35.5	14.0	21.7	Mean	37.7	11.8	22.8
	BJF	24.0	5.0	13.0	CHU	26.5	3.5	12.5
WHU	GUA	20.5	3.0	11.5	KUN	33.0	3.5	15.0
	SHA	27.5	11.0	18.3	WUH	26.0	6.0	14.8
	XIA	30.5	5.0	16.0	Mean	26.9	5.3	14.4

305

4.2.2 Positioning accuracy of RT-PPP

306

The positioning accuracies of RT-PPP for each analysis center at the seven IGMAS stations are evaluated.

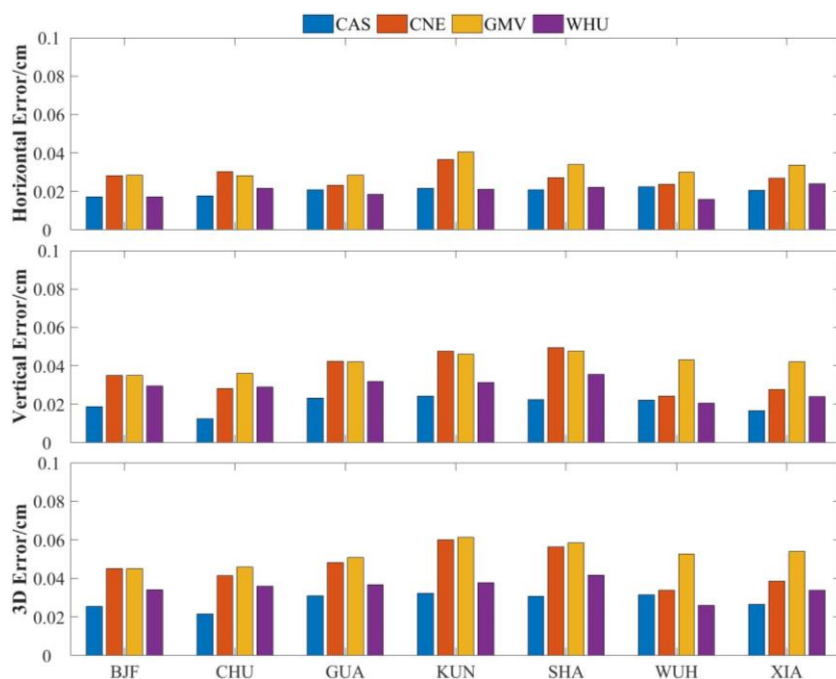
307

Figure 9 shows the positioning accuracies in horizontal, vertical, and 3D directions. CAS exhibits the highest

308

accuracy, with 2.1, 2.4, and 3.2 cm in three aspects, respectively. Then, WHU shows a 3.3 cm accuracy in

309 the 3D direction, which is similar to the positioning accuracy of CAS. Since the RMSEs of the SSR products
 310 from CNE are higher than those of CAS and WHU, the PPP-performance based on CNE is unsatisfactory
 311 than CAS and WHU. The positioning accuracy with GMV is the worst compared with other analysis centers.
 312 The positioning performances of RT-PPP based on GMV-SSR products are 3.2 cm in horizontal directions
 313 and 4.2 cm in vertical directions. The mean RMSE of 3D positioning accuracy exceeds 5 cm, which is all
 314 higher than those of the remaining three analysis centers. Therefore, the combination with BeiDou satellite
 315 can improve the positioning performance of RT-PPP.



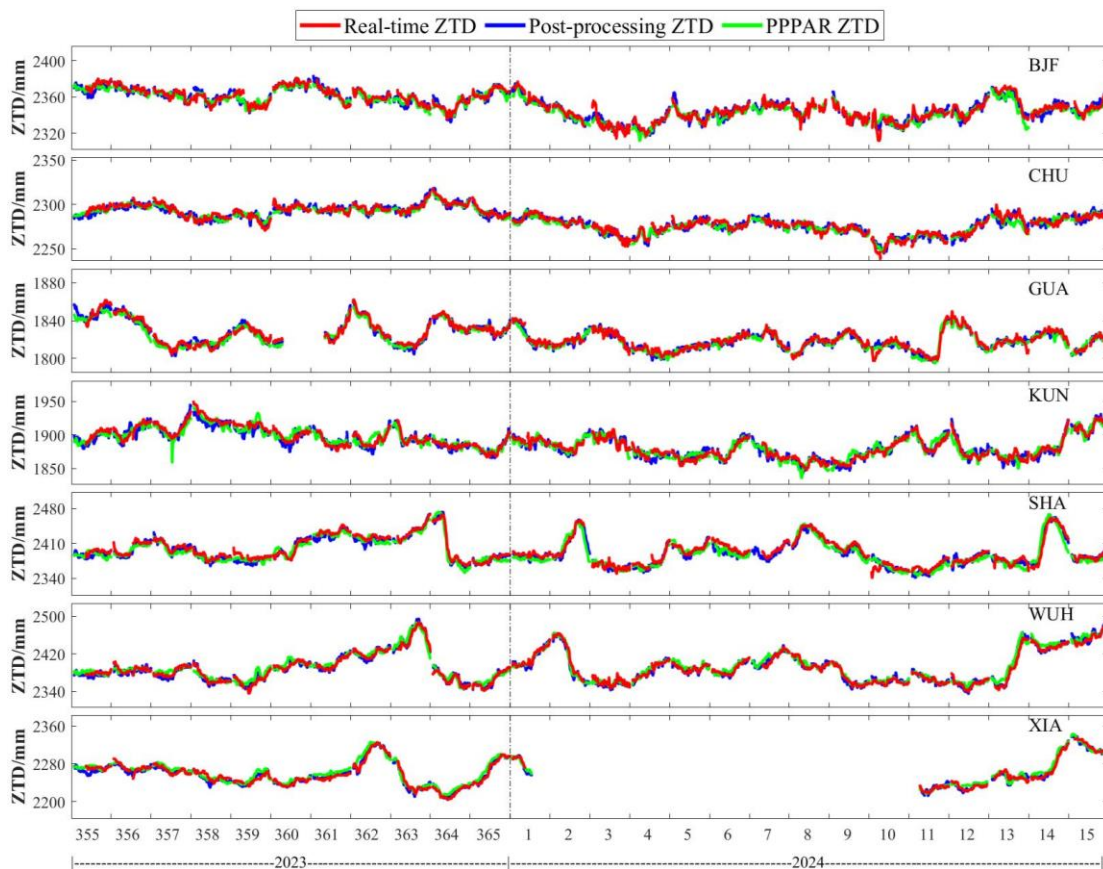
316
 317 Figure 9. The positioning accuracies in horizontal, vertical, and 3D directions of different analysis centers
 318 at seven IGMAS stations.

319 4.3 Accuracy of RT-PPP-derived ZTD

320 4.3.1 Accuracy of RT-PPP-derived ZTDs obtained by different SSR products

321 RT-PPP-derived ZTDs based on four analysis center SSR products are compared with post-processing
 322 PPP and PRIDE PPPAR-derived ZTDs, respectively, to verify the accuracy of RT-PPP ZTD retrieval. Figure
 323 10 shows timing diagrams for RT-PPP-derived ZTDs obtained by WHU-SSR products alongside those of
 324 PRIDE PPPAR and post-processing PPP-derived ZTDs. RT-PPP, post-processing PPP, and PRIDE PPPAR-
 325 derived ZTDs have a similar trend. Table 9 shows the differences of RT-PPP-derived ZTDs versus PRIDE
 326 PPPAR-derived ZTDs for each analysis center at the seven IGMAS stations. The GUA station lacked
 327 observation data from 7:00 AM on DOY 360 to 7:00 AM on DOY 361 in 2023. And the XIA station lacked
 328 observation data from 1:00 PM on DOY 1 to 5:00 AM on DOY 11 in 2024. The "breakpoints" in Figure 10
 329 are caused by occasional disconnections between the local network and the mount-point, which result in data
 330 loss. RT-PPP-derived ZTDs accuracies for GMV can be reached centimeter level. Furthermore, the average
 331 accuracies of RT-PPP-derived ZTDs for CAS, WHU, and CNE reach the millimeter level. RT-PPP-derived

332 ZTDs based on WHU have the highest ZTD accuracy with an RMSE of 6.06 mm. CAS and WHU exhibit
 333 similar ZTD accuracies with 6.80 mm. The accuracy of RT-PPP-derived ZTDs based on GMV-SSR products
 334 is the worst, with 10.30 mm. The accuracy of RT-PPP-derived ZTDs based on GMV is worse than the other
 335 analysis centers, probably because GMV does not provide BDS3 SSR products. The STDs of each analysis
 336 center are similar to the RMSEs, with WHU being the best, CAS being slightly inferior, and GMV being the
 337 worst. The bias of four analysis centers exhibits minimal differences with around 2.30 mm. The average R
 338 of four analysis centers exceed 0.9, with 0.96/0.93/0.93/0.97, respectively, indicating that RT-PPP-derived
 339 ZTD strongly correlates with PRIDE PPPAR-derived ZTD. The result of RT-PPP-derived ZTD versus post-
 340 processing PPP-derived ZTD is similar. The order of RMSEs and STDs for different analysis centers is
 341 GMV>CNE>CAS>WHU. The average R of four analysis centers also exceed 0.9 with 0.96/0.95/0.91/0.97,
 342 respectively. In summary, the accuracy of RT-PPP ZTD retrieval obtained by WHU-SSR products is the best.



343

344 Figure 10. RT-PPP, post-processing PPP, and PRIDE PPPAR-derived ZTDs at IGMAS stations.

345

346 Table 9. The accuracies of RT-PPP-derived ZTDs from different analysis centers at seven IGMAS

346

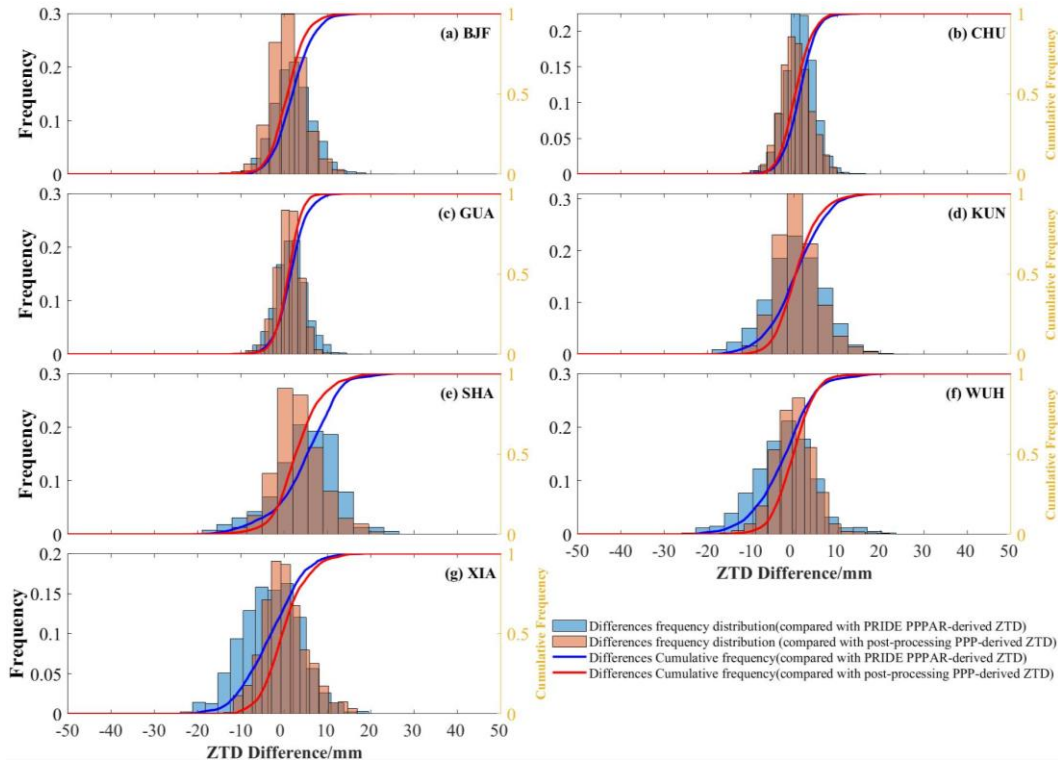
stations/mm.

analysis center	Station	RMS E	STD	Bias	R	analysis center	Station	RMS E	STD	Bias	R
CAS	BJF	7.01	6.57	2.44	0.94	CNE	BJF	7.92	7.04	3.62	0.92
	CHU	3.25	3.21	0.49	0.98		CHU	5.04	4.75	1.68	0.95
	GUA	4.01	3.49	1.97	0.98		GUA	5.62	5.57	0.73	0.93

	KUN	7.23	7.08	-1.47	0.97		KUN	9.73	9.17	3.26	0.91
	SHA	9.2	7.14	5.8	0.94		SHA	13.03	11.1	6.82	0.93
	WUH	9.96	8.65	-4.95	0.97		WUH	11	10.38	-3.65	0.96
	XIA	7	5.99	3.61	0.98		XIA	8.02	7.83	1.71	0.97
	Mean	6.80	6.01	1.12	0.96		Mean	8.62	7.97	2.02	0.93
GMV	BJF	10	10	0.27	0.91	WHU	BJF	4.98	4.46	2.21	0.96
	CHU	6.75	6.19	2.69	0.96		CHU	3.58	3.35	1.26	0.98
	GUA	8.09	6.7	4.53	0.95		GUA	3.79	3.45	1.57	0.97
	KUN	9.12	9	1.46	0.91		KUN	6.4	6.38	0.51	0.95
	SHA	13.47	11.03	7.73	0.94		SHA	8.94	7.49	4.91	0.97
	WUH	12.78	12.69	-1.47	0.95		WUH	7.42	7.01	-2.42	0.98
	XIA	11.95	11.93	0.61	0.94		XIA	7.33	6.68	3.02	0.98
	Mean	10.30	9.64	2.26	0.93		Mean	6.06	5.54	1.58	0.97

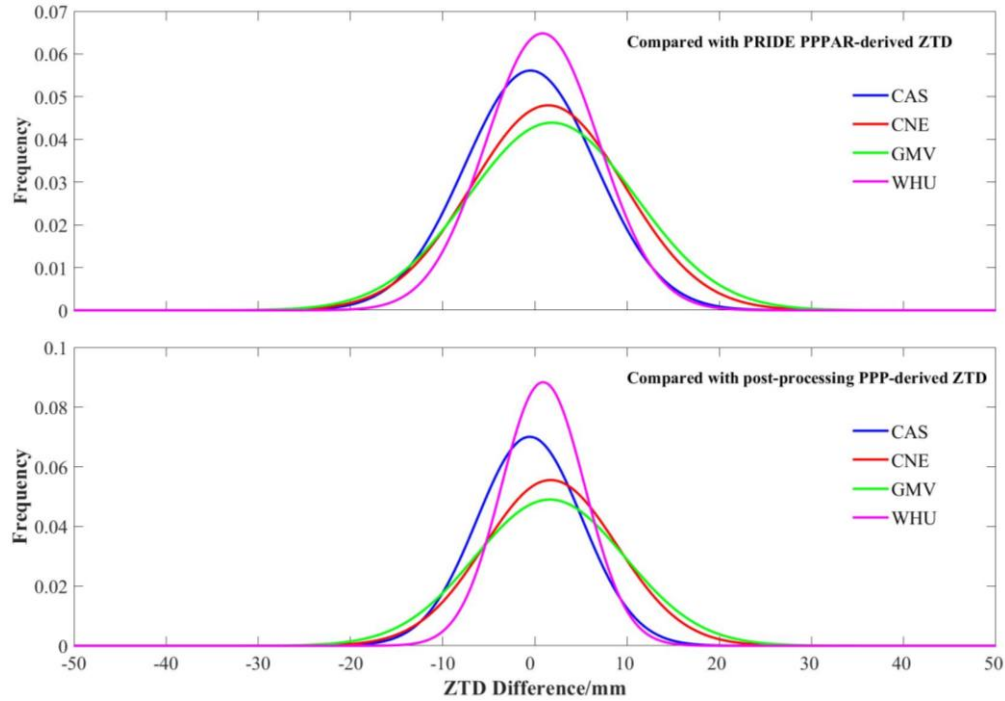
347

348 The differences of RT-PPP-derived ZTD versus PRIDE PPPAR and post-processing PPP-derived ZTD
349 are counted separately to further analyze the ZTD consistency, respectively. Figure 11 shows the differences
350 distribution of RT-PPP compared with PRIDE PPPAR and post-processing PPP-derived ZTDs, respectively,
351 where the bar graph shows the differences frequency distribution and the curve shows the differences
352 cumulative frequency. The differences frequency of RT-PPP-derived ZTDs versus PRIDE PPPAR and post-
353 processing PPP-derived ZTDs at the seven stations are normally distributed, respectively. The bias of RT-
354 PPP-derived ZTDs at all stations is nearly 0 mm. The differences distribution of RT-PPP-derived ZTDs based
355 on the other analysis centers are also counted, and the bias is nearly 0 mm. Figure 12 shows the error
356 distribution for the four analysis centers. It is evident that the error distributions of ZTD inversion from all
357 four centers follow a normal distribution, with the STDs of the ZTD derived from WHU being notably smaller
358 than that of the other centers. Therefore, the measure of dispersion of RT-PPP-derived ZTDs based on WHU
359 is lower than CAS, CNE, GMV. RT-PPP-derived ZTDs based WHU SSR products have the best ZTD
360 retrieval accuracy. The result is consistent with the conclusion of 3.2.1.



361
362
363

Figure 11. The differences distribution of RT-PPP-derived ZTDs compared with post-processing PPP and PRIDE PPPAR-derived ZTDs.

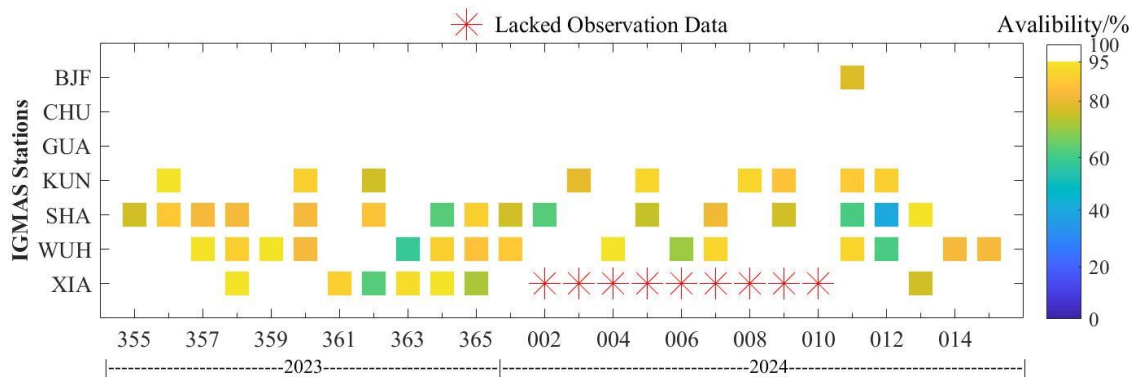


364
365

Figure 12. The differences distribution of RT-PPP-derived ZTDs based on four analysis centers.

366 4.3.2 RT-ZTD availability

367 The availability of RT-PPP-derived ZTD is assessed. RT-PPP-derived ZTD in the epoch is considered
 368 unavailable if the differences of RT-PPP-derived ZTD versus PRIDE PPPAR and post-processing PPP-
 369 derived ZTD in arbitrary epoch are more than 10 mm, respectively. The daily availability of RT-PPP-derived
 370 ZTD based on WHU-SSR products is calculated (Figure 12). Daily ZTD availability of sites with less ZTD
 371 variations can be maintained at more than 95%, such as BJF, CHU, and GUA. Daily ZTD availability of sites
 372 with large ZTD variations can basically be maintained at more than 80%. A similar result also appears in the
 373 comparison between RT-PPP-derived ZTD and post-processing PPP-derived ZTD. Table 10 shows the
 374 availability of RT-PPP-derived ZTD for the four SSR products at the seven stations using PRIDE PPPAR-
 375 derived ZTD as references. RT-PPP-derived ZTDs based on WHU-SSR products have the highest
 376 availability, with an average availability of 89% at all stations. The ZTD availability of CAS is slightly lower
 377 with 85% and CNE is lower than CAS and WHU with 78%. GMV shows the worst availability with 70%.
 378 The ZTD availability is positively correlated with the SISRE of SSR products from different analysis centers.
 379 Therefore, the SSR products provided by WHU effectively support high-precision RT-PPP ZTD retrieval.



380
 381 Figure 13. The availability of RT-PPP-derived ZTDs from WHU SSR products at seven IGMAS
 382 stations/%.

383 Table 10. The availability of RT-PPP-derived ZTDs from different analysis center products at IGMAS
 384 stations/%.

analysis center	BJF	CHU	GUA	KUN	SHA	WUH	XIA	sum
CAS	91	99	97	83	74	72	79	85
CNE	83	95	92	71	57	69	80	78
GMV	75	87	80	77	51	58	62	70
WHU	97	99	98	90	77	85	82	89

385 5 CONCLUSIONS

386 Evaluating the accuracies of RT-PPP-derived ZTD based on SSR products from different analysis centers
 387 is crucial in warning and forecasting extreme natural disasters and earth observation error correction. In this
 388 study, the accuracies of GPS, Galileo, and BDS3 RT satellite orbit and clock error products from four analysis
 389 centers are evaluated. Then the positioning performance and ZTD accuracies for multi-GNSS RT-PPP are

390 assessed. The following conclusions are obtained. The average epoch availability of SSR corrections
391 provided by four analysis centers exceeds 97.5%, and CAS-SSR products have the highest satellite
392 availability. CAS has the best SISREs of GPS, Galileo, and BDS3, followed by WHU, while CNE and GMV
393 exhibit the worst performance. The results of multi-GNSS RT-PPP indicate that WHU achieves the shortest
394 average convergence times with 14.4 min, followed by CAS and CNE. The average convergence time of
395 GMV is 22.8 min, significantly lower than other analysis centers. The accuracies of RT-PPP-derived ZTD
396 obtained by four analysis centers are better than 11 mm, and RT-PPP-derived ZTD is in good conformity
397 with PRIDE PPPAR-derived ZTD. Among the four analysis centers, WHU has the best accuracy of RT-PPP-
398 derived ZTD with an average RMSE of 6.1 mm, and RT-PPP-derived ZTD based on WHU SSR products
399 has the highest availability with 89%. This study is essential for selecting SSR products from different
400 analysis centers for RT-PPP ZTD retrieval.

401

402

403 **Data and code availability**

404 The IGMAS GNSS data are available from Wuhan University, but restrictions apply to the availability of
405 these data, which were used under licence for the current study and so are not publicly available. The data
406 are, however, available from the authors upon reasonable request and with the permission of Wuhan
407 University. Post-processing products and GNSS data from IGS are available at
408 <https://cddis.nasa.gov/archive/gnss/>. Post-processing products and GNSS data from IGS are available at
409 ntrip.gnsslab.cn.

410

411 **Author contributions**

412 WQY and HRH provided the initial idea and designed the experiments for this study; QZ guided the entire
413 process of this study; XWM and QZ analyzed the data and wrote the manuscript; YBY, XHL, QZZ and YZH
414 helped with the writing. All authors reviewed the manuscript.

415

416 **Competing interests**

417 The authors declare that they have no known competing financial interests or personal relationships that
418 could have influenced the work reported in this study.

419

420 **Disclaimer**

421 Publisher's note: Copernicus Publications remains neutral with regard to jurisdictional claims made in the
422 text, published maps, institutional affiliations, or any other geographical representation in this paper. While
423 Copernicus Publications makes every effort to include appropriate place names, the final responsibility lies
424 with the authors.

425

426 **Acknowledgments**

427 The reviewers' and editors' comments are highly appreciated. We thank IGMAS and IGS for providing
428 GNSS data for this analysis. We also thank IGS for providing the SSR products and precision products.

429

430 **Funding**

431 This work was supported by the State Key Laboratory of Geodesy and Earth's Dynamics, Innovation
432 Academy for Precision Measurement Science and Technology, Chinese Academy of Sciences
433 (SKLGED2024-3-8), the National Natural Science Foundation of China (42330105), the National Natural
434 Science Foundation of China (42201484), also in part by Key Laboratory of Mine Geological Hazards
435 Mechanism and Control, Ministry of Natural Resources (6000230168), and China Postdoctoral Science
436 Foundation (2023MD744243).

437

438 **Author details**

439 ¹Wanqiang Yao, Haoran Huang, Xiongwei Ma, Xiaohu Lin, Qingzhi Zhao, Yunzheng Huang are with the
440 College of Geomatics, Xi'an University of Science and Technology, Xi'an 710054, China, (e-mail:
441 sxywq@163.com; huanghr0213@163.com; xiongw_ma@xust.edu.cn; xhlin214@xust.edu.cn;
442 zhaoqingzhia@163.com; huangyunzheng0527@163.com).

443 ²Qi Zhang, Yibin Yao are with the School of Geodesy and Geomatics, Wuhan University. Wuhan 430000,
444 China. (e-mail: qizhangsgg@whu.edu.cn; ybyao@whu.edu.cn).

445

446 **References**

- 447 Alcay, S., and Turgut, M.: Evaluation of the positioning performance of multi-GNSS RT-PPP method, Arab.
448 J. Geosci., 14, 1-19, <https://doi.org/10.1007/s12517-021-06534-4>, 2021.
- 449 Capilla, R. M., Berné, J. L., Martín, A., and Rodrigo, R.: Simulation case study of deformations and landslides
450 using real-time GNSS precise point positioning technique, Geomat. Nat. Haz. Risk., 7, 1856-1873,
451 <https://doi.org/10.1080/19475705.2015.1137243>, 2016.
- 452 Crocetti, L., Schartner, M., Zus, F., Zhang, W., Moeller, G., Navarro, V., See, L., Schindler, K., and Soja, B.:
453 Global, spatially explicit modelling of zenith wet delay with XGBoost, J. Geodesy., 98, 23,
454 <https://doi.org/10.1007/s00190-024-01829-2>, 2024.
- 455 Di, M.-W., Zhang, A.-M., Guo, B.-F., Zhang, J.-L., Liu, R.-X., and Li, M.-Y.: Evaluation of real-time PPP-
456 based tide measurement using IGS real-time service, Sensors, 20, 2968,
457 <https://doi.org/10.3390/s20102968>, 2020.
- 458 Edokossi, K., Calabria, A., Jin, S., and Molina, I.: GNSS-reflectometry and remote sensing of soil moisture:
459 A review of measurement techniques, methods, and applications, Remote Sensing, 12, 614,
460 <https://doi.org/10.3390/rs12040614>, 2020.
- 461 Elsobeiey, M., and Al-Harbi, S.: Performance of real-time Precise Point Positioning using IGS real-time
462 service, GPS solutions, 20, 565-571, <https://doi.org/10.1007/s10291-015-0467-z>, 2016.

- 463 Eugenia Bianchi, C., Oscar Mendoza, L. P., Isabel Fernandez, L., Paula Natali, M., Margarita Meza, A., and
464 Francisco Moirano, J.: Multi-year GNSS monitoring of atmospheric IWV over Central and South
465 America for climate studies, *Ann. Geophys.*, 34, 623-639, [https://doi.org/10.5194/angeo-34-623-](https://doi.org/10.5194/angeo-34-623-2016)
466 2016, 2016.
- 467 Gao, M.-Y., Xu, C.-J., and Liu, Y.: Evaluation of Time-Series InSAR Tropospheric Delay Correction
468 Methods over Northwestern Margin of the Qinghai-Tibet Plateau, *Geomatics and Information*
469 *Science of Wuhan University*, 46, 1548-1559, <https://doi.org/10.1016/j.scitotenv.2024.170875>,
470 2021.
- 471 Ge, Y.-L., Chen, S.-X., Wu, T., Fan, C.-M., Qin, W.-J., Zhou, F., and Yang, X.-H.: An analysis of BDS-3
472 real-time PPP: Time transfer, positioning, and tropospheric delay retrieval, *Measurement*, 172,
473 108871, <https://doi.org/10.1016/j.measurement.2020.108871>, 2021.
- 474 Geng, J.-H., Yang, S.-F., and Guo, J.: Assessing IGS GPS/Galileo/BDS-2/BDS-3 phase bias products with
475 PRIDE PPP-AR, *Satellite Navigation*, 2, 1-15, <https://doi.org/10.1186/s43020-021-00049-9>, 2021.
- 476 Griffiths, J.: Combined orbits and clocks from IGS second reprocessing, *J. Geodesy.*, 93, 177-195,
477 <https://doi.org/10.1007/s00190-018-1149-8>, 2019.
- 478 Gu, S.-F., Guo, R.-X., Gong, X.-P., Zhang, S.-C., Lou, Y.-D., and Li, Z.-H.: Real-time precise point
479 positioning based on BDS-3 global short message communication, *GPS Solutions*, 26, 107,
480 <https://doi.org/10.1007/s10291-022-01291-7>, 2022.
- 481 Hadas, T., Hobiger, T., and Hordyniec, P.: Considering different recent advancements in GNSS on real-time
482 zenith troposphere estimates, *GPS Solutions*, 24, 99, <https://doi.org/10.1007/s10291-020-01014-w>,
483 2020.
- 484 He, L., Yao, Y.-B., Xu, C.-Q., Zhang, H., Tang, F.-F., Ji, C.-Q., Liu, Z., and Wu, W.-T.: A New Global ZTD
485 Forecast Model Based on Improved LSTM Neural Network, *IEEE. J-STARS.*,
486 <https://doi.org/10.1109/JSTARS.2024.3391821>, 2024.
- 487 Jiao, G.-Q., Song, S.-L., Ge, Y.-L., Su, K., and Liu, Y.-Y.: Assessment of BeiDou-3 and multi-GNSS precise
488 point positioning performance, *Sensors*, 19, 2496, <https://doi.org/10.3390/s19112496>, 2019.
- 489 Ju, B.-X., Jiang, W.-P., Tao, J., Hu, J.-L., Xi, R.-J., Ma, J., and Liu, J.-N.: Performance evaluation of GNSS
490 kinematic PPP and PPP-IAR in structural health monitoring of bridge: Case studies, *Measurement*,
491 203, 112011, <https://doi.org/10.1016/j.measurement.2022.112011>, 2022.
- 492 Kazmierski, K., Zajdel, R., and Sońnica, K.: Evolution of orbit and clock quality for real-time multi-GNSS
493 solutions, *GPS solutions*, 24, 111, <https://doi.org/10.1007/s10291-020-01026-6>, 2020.
- 494 Ke, S., and Shuanggen, J.: Analysis and comparisons of the BDS/Galileo quad-frequency PPP models
495 performances, *Acta Geodaetica et Cartographica Sinica*, 49, 1189,
496 <https://doi.org/10.11947/j.AGCS.2020.20200236>, 2020.
- 497 Kinoshita, Y.: Development of InSAR neutral atmospheric delay correction model by use of GNSS ZTD and
498 its horizontal gradient, *IEEE T. Geosci. Remote.*, 60, 1-14,
499 <https://doi.org/10.1109/TGRS.2022.3188988>, 2022.

- 500 Li, B.-F., Ge, H.-B., Bu, Y.-H., Zheng, Y.-N., and Yuan, L.-T.: Comprehensive assessment of real-time
501 precise products from IGS analysis centers, *Satellite Navigation*, 3, 12,
502 <https://doi.org/10.1186/s43020-022-00074-2>, 2022.
- 503 Li, H.-B., Choy, S., Wang, X.-M., Liang, H., and Zhang, K.-F.: Monitoring the migration of water vapor
504 using ground-based GNSS tropospheric products, *IEEE Geosci. Remote. S.*, 20, 1-5,
505 <https://doi.org/10.1109/LGRS.2023.3282362>, 2023.
- 506 Li, H.-B., Choy, S., Wang, X.-M., Zhang, K.-F., Jiang, C.-H., Li, L.-Q., Liu, X., Hu, A.-D., Wu, S.-Q., and
507 Zhu, D.-J.: Estimation of diurnal-provided potential evapotranspiration using GNSS and
508 meteorological products, *Atmos. Res.*, 280, 106424,
509 <https://doi.org/10.1016/j.atmosres.2022.106424>, 2022.
- 510 Li, H.-B., Choy, S., Zaminpardaz, S., Carter, B., Sun, C., Purwar, S., Liang, H., Li, L.-Q., and Wang, X.-M.:
511 Investigating the inter-relationships among multiple atmospheric variables and their responses to
512 precipitation, *Atmosphere*, 14, 571, <https://doi.org/10.3390/atmos14030571>, 2023.
- 513 Li, H.-B., Wang, X.-M., Choy, S., Wu, S.-Q., Jiang, C.-H., Zhang, J.-L., Qiu, C., Li, L., and Zhang, K.-F.: A
514 new cumulative anomaly-based model for the detection of heavy precipitation using GNSS-derived
515 tropospheric products, *IEEE T. Geosci. Remote.*, 60, 1-18,
516 <https://doi.org/10.1109/TGRS.2021.3137014>, 2021.
- 517 Li, R.-H., Zhang, Z.-J., Gao, Y., Zhang, J.-Y., and Ge, H.-B.: A New Method for Deformation Monitoring
518 of Structures by Precise Point Positioning, *Remote Sensing*, 15, 5743,
519 <https://doi.org/10.3390/rs15245743>, 2023.
- 520 Li, S., Jiang, N., Xu, T.-H., Xu, Y., Yang, H.-L., Zhang, Z., Guo, A., and Wu, Y.-H.: A precipitation forecast
521 model with a neural network and improved GPT3 model for Japan, *GPS Solutions*, 27, 186,
522 <https://doi.org/10.1007/s10291-023-01526-1>, 2023.
- 523 Li, X.-X., Dick, G., Lu, C.-X., Ge, M.-R., Nilsson, T., Ning, T., Wickert, J., and Schuh, H.: Multi-GNSS
524 meteorology: real-time retrieving of atmospheric water vapor from BeiDou, Galileo, GLONASS,
525 and GPS observations, *IEEE T. Geosci. Remote.*, 53, 6385-6393,
526 <https://doi.org/10.1109/TGRS.2015.2438395>, 2015.
- 527 Li, X.-X., Wang, Q.-Y., Wu, J.-Q., Yuan, Y.-Q., Xiong, Y., Gong, X.-W., and Wu, Z.-L.: Multi-GNSS
528 products and services at iGMAS Wuhan Innovation Application Center: Strategy and evaluation,
529 *Satellite Navigation*, 3, 20, <https://doi.org/10.1186/s43020-022-00081-3>, 2022.
- 530 Lin, C. Y., Deng, Y., and Ridley, A.: Atmospheric gravity waves in the ionosphere and thermosphere during
531 the 2017 solar eclipse, *Geophys. Res. Lett.*, 45, 5246-5252, <https://doi.org/10.1029/2018GL077388>,
532 2018.
- 533 Liu, T., Zhang, B.-C., Yuan, Y.-B., and Li, M.: Real-Time Precise Point Positioning (RTPPP) with raw
534 observations and its application in real-time regional ionospheric VTEC modeling, *J. Geodesy.*, 92,
535 1267-1283, <https://doi.org/10.1007/s00190-018-1118-2>, 2018.

- 536 Lu, C.-X., Chen, X.-H., Liu, G., Dick, G., Wickert, J., Jiang, X.-Y., Zheng, K., and Schuh, H.: Real-time
537 tropospheric delays retrieved from multi-GNSS observations and IGS real-time product streams,
538 *Remote Sensing*, 9, 1317, <https://doi.org/10.3390/rs9121317>, 2017.
- 539 Lu, C.-X., Li, X.-X., Ge, M.-R., Heinkelmann, R., Nilsson, T., Soja, B., Dick, G., and Schuh, H.: Estimation
540 and evaluation of real-time precipitable water vapor from GLONASS and GPS, *GPS solutions*, 20,
541 703-713, <https://doi.org/10.1007/s10291-015-0479-8>, 2016.
- 542 Lu, C.-X., Li, X.-X., Nilsson, T., Ning, T., Heinkelmann, R., Ge, M.-R., Glaser, S., and Schuh, H.: Real-time
543 retrieval of precipitable water vapor from GPS and BeiDou observations, *J. Geodesy.*, 89, 843-856,
544 <https://doi.org/10.1007/s00190-015-0818-0>, 2015.
- 545 Ma, X.-W., Zhao, Q.-Z., Yao, Y.-B., and Yao, W.-Q.: A novel method of retrieving potential ET in China, *J.*
546 *Hydrol.*, 598, 126271, <https://doi.org/10.1016/j.jhydrol.2021.126271>, 2021.
- 547 Pan, L., Deng, M., and Chen, B.-Y.: Real-time GNSS meteorology: a promising alternative using real-time
548 PPP technique based on broadcast ephemerides and the open service of Galileo, *GPS Solutions*, 28,
549 113, <https://doi.org/10.1007/s10291-024-01659-x>, 2024.
- 550 Pan, L., and Guo, F.: Real-time tropospheric delay retrieval with GPS, GLONASS, Galileo and BDS data,
551 *Sci. Rep.*, 8, 17067, <https://doi.org/10.1038/s41598-018-35155-3>, 2018.
- 552 Pipatsitee, P., Ninsawat, S., Tripathi, N. K., Shanmugam, M., and Chitsutti, P.: Estimating daily potential
553 evapotranspiration using GNSS-based precipitable water vapor, *Heliyon*, 9,
554 <https://doi.org/10.1016/j.heliyon.2023.e17747>, 2023.
- 555 Sha, Z.-M., Hu, F.-X., Wei, P.-Z., Ye, S.-R., and Zhu, Y.-X.: A method for calculating real-time ZTD grid
556 data in Chinese regions based on GNSS ZTD modified ERA5 grid products, *J. Atmos. Sol.-Terr.*
557 *Phy.*, 255, 106174, <https://doi.org/10.1016/j.jastp.2024.106174>, 2024.
- 558 Shu, B., Tian, Y.-Q., Qu, X.-Y., Li, P., Wang, L., Huang, G.-W., Du, Y., and Zhang, Q.: Estimation of BDS-
559 2/3 phase observable-specific signal bias aided by double-differenced model: an exploration of fast
560 BDS-2/3 real-time PPP, *GPS solutions*, 28, 1-14, <https://doi.org/10.1007/s10291-024-01632-8>,
561 2024.
- 562 Stepniak, K., Bock, O., Bosser, P., and Wielgosz, P.: Outliers and uncertainties in GNSS ZTD estimates from
563 double-difference processing and precise point positioning, *GPS Solutions*, 26, 74,
564 <https://doi.org/10.1007/s10291-022-01261-z>, 2022.
- 565 Su, C.-Y., Shu, B., Zheng, L., Tian, Y.-Q., Lei, T.-J., Mu, X.-F., and Wang, L.: Quality evaluation and PPP
566 performance analysis of GPS/BDS real-time SSR products, *Geomatics and Information Science of*
567 *Wuhan University*, <https://doi.org/10.13203/j.whugis20220760>, 2023.
- 568 Teunissen, P., Odolinski, R., and Odijk, D.: Instantaneous BeiDou+ GPS RTK positioning with high cut-off
569 elevation angles, *Journal of geodesy*, 88, 335-350, <https://doi.org/10.1007/s00190-013-0686-4>,
570 2014.

- 571 Wang, D., Huang, G.-W., Du, Y., Zhang, Q., Bai, Z.-W., and Tian, J.: Stability analysis of reference station
572 and compensation for monitoring stations in GNSS landslide monitoring, *Satellite Navigation*, 4,
573 29, <https://doi.org/10.1186/s43020-023-00119-0>, 2023.
- 574 Wang, L., Li, Z.-S., Ge, M.-R., Neitzel, F., Wang, Z.-Y., and Yuan, H.: Validation and assessment of multi-
575 GNSS real-time precise point positioning in simulated kinematic mode using IGS real-time service,
576 *Remote Sensing*, 10, 337, <https://doi.org/10.3390/rs10020337>, 2018.
- 577 Wang, Z.-Y., Li, Z.-S., Wang, L., Wang, X.-M., and Yuan, H.: Assessment of multiple GNSS real-time SSR
578 products from different analysis centers, *ISPRS Int. J. Geo.-Inf.*, 7, 85,
579 <https://doi.org/10.3390/ijgi7030085>, 2018.
- 580 Xiong, Z.-H., Zhang, B., and Yao, Y.-B.: Comparisons between the WRF data assimilation and the GNSS
581 tomography technique in retrieving 3-D wet refractivity fields in Hong Kong, *Ann. Geophys.*, 37,
582 25-36, <https://doi.org/10.5194/angeo-37-25-2019>, 2019.
- 583 Yao, Y.-B., He, Y.-D., Yi, W.-T., Song, W.-W., Cao, C., and Chen, M.: Method for evaluating real-time
584 GNSS satellite clock offset products, *GPS Solutions*, 21, 1417-1425,
585 <https://doi.org/10.1007/s10291-017-0619-4>, 2017.
- 586 Yao, Y.-B., Luo, Y.-Y., Zhang, J.-Y., and Zhao, C.-J.: Correlation analysis between haze and GNSS
587 tropospheric delay based on coherent wavelet, *Geomatics and Information Science of Wuhan*
588 *University*, 43, 2131-2138, <https://doi.org/10.13203/j.whugis20180234>, 2018.
- 589 Zhang, Z.-T., Zeng, P., Wen, Y.-L., He, L.-N., and He, X.-F.: Comprehensive assessment of BDS-2 and
590 BDS-3 precise orbits based on B1I/B3I and B1C/B2a frequencies from iGMAS, *Remote Sensing*,
591 15, 582, <https://doi.org/10.3390/rs15030582>, 2023.
- 592 Zhu, G., Huang, L.-K., Yang, Y.-Z., Li, J.-Y., Zhou, L., and Liu, L.-L.: Refining the ERA5-based global
593 model for vertical adjustment of zenith tropospheric delay, *Satellite Navigation*, 3, 27,
594 <https://doi.org/10.1186/s43020-022-00088-w>, 2022.
- 595
- 596

